Mineralogic constraints on sulfur-rich soils from Pancam spectra at Gusev crater, Mars

J. R. Johnson,[1] J. F. Bell III,[2] E. Cloutis,[3] M. Staid,[4] W. H. Farrand,[5] T. McCoy,[6] M. Rice,[2] A. Wang,[7] and A. Yen[8]

[1] The Mars Exploration Rover (MER) Spirit excavated sulfur-rich soils exhibiting high albedo and relatively white to yellow colors at three main locations on and south of Husband Hill in Gusev crater, Mars. The multispectral visible/near-infrared properties of these disturbed soils revealed by the Pancam stereo color camera vary appreciably over small spatial scales, but exhibit spectral features suggestive of ferric sulfates. Spectral mixture models constrain the mineralogy of these soils to include ferric sulfates in various states of hydration, such as ferricopiapite $[Fe_{2/3}^{2+}Fe_4^{3+}(SO_4)_6(OH)_2 \cdot 20(H_2O)]$, hydronium jarosite $[(H_3O)Fe_3^{3+}(SO_4)_2(OH)_6]$, fibroferrite $[Fe^{3+}(SO_4)(OH) \cdot 5(H_2O)]$, rhomboclase $[HFe^{3+}(SO_4)_2 \cdot 4(H_2O)]$, and paracoquimbite $[Fe_2^{3+}(SO_4)_3 \cdot 9(H_2O)]$. **Citation:** Johnson, J. R., J. F. Bell III, E. Cloutis, M. Staid, W. H. Farrand, T. McCoy, M. Rice, A. Wang, and A. Yen (2007), Mineralogic constraints on sulfur-rich soils from Pancam spectra at Gusev crater, Mars, *Geophys. Res. Lett.*, *34*, L13202, doi:10.1029/2007GL029894.

1. Introduction

[2] Three major occurrences of light-toned soils were encountered by the Mars Exploration Rover (MER) Spirit after its wheels had excavated subsurface materials: (1) near a region named "Paso Robles" on Husband Hill on Martian day ("Sol") 400; (2) south of Husband Hill in a feature named "Arad" on Sol 721; and (3) near Home Plate at a region named "Tyrone" on Sol 790. Where these disturbed soils were least contaminated by contributions from typical reddish surface soils, they exhibited high albedos with white to yellow hues that varied over small length scales (Figure 1). Observations by the Alpha Particle X-ray Spectrometer (APXS) showed high sulfur contents (up to 35 wt. % SO_3), and Mössbauer spectrometer measurements suggested that the soils included ferric-bearing sulfates [*Gellert et al.*, 2006; *Morris et al.*, 2006; *Ming et al.*, 2006; *Wang et al.*, 2006].

Mini-TES measurements suggested the presence of a 6 μm bound water spectral feature, consistent with the presence of hydrated minerals, particularly for the Tyrone soils [*Lane et al.*, 2006b; S. Ruff, personal communication, 2006].

[3] Pancam spectra of these materials exhibited distinctive reflectance maxima near 670 nm consistent with the presence of hydrated ferric sulfates. Subtle absorptions between 800–860 nm were observed in some spectra (Figure 2), also consistent with some sulfate minerals [cf. *Bishop et al.*, 2006; *Lane et al.*, 2007, *Parente et al.*, 2007]. The objective of this work is to constrain the mineralogy of these soils by modeling their Pancam visible/near-infrared spectra using linear mixing models and spectral libraries that include a suite of well-characterized minerals.

2. Methods

2.1. Pancam Spectra

[4] The two cameras comprising the Pancam instrument each use 1024 × 1024 pixel charge-coupled devices (CCDs) with a 30 cm stereo separation and 0.27 mrad per pixel resolution [*Bell et al.*, 2003, 2006]. Pancam includes 13 narrowband filters covering 11 unique wavelengths from 434 to 1009 nm. Measurements of the Pancam calibration target, pre-launch calibration data and modeling were used to convert raw image counts to calibrated radiance and then to radiance factor (I/F, where I is the measured radiance and πF is the incident solar irradiance [*Bell et al.*, 2003, 2006; *Sohl-Dickstein et al.*, 2005]). The original 12-bit per pixel (bpp) Pancam image data were compressed using a combination of 12 to 8 bit square-root encoding and a wavelet-based image compression technique [*Maki et al.*, 2003; *Bell et al.*, 2003, 2006]. The Paso Robles and Arad data sets were compressed so that 434 nm stereo bands were compressed losslessly and all other bands were compressed to an effective rate of 2 bpp ($\sim$6:1 compression ratio). The Tyrone data were acquired at 2 bpp for the 434 nm bands, and 1 bpp ($\sim$12:1) for all other bands. Compression effects on radiometric precision were estimated to be <1% based on pre-launch tests [*Bell et al.*, 2006].

[5] Spectra were extracted by manually selecting pixels from common areas in both left and right eye data sets. Selected regions of interest are shown in Figure 1, and details on image sequences are presented in Table 1. Spectra were combined by normalizing I/F values from the same surface regions in the red stereo bands (753 and 754 nm) to their average, and dividing by *cos*(solar incidence) to provide relative reflectance (R*) [*Reid et al.*, 1999; *Bell et al.*, 2006]. Relative filter-to-filter uncertainties in R* were estimated as 1–5% and absolute reflectance levels are accurate to $\sim$10% [*Bell et al.*, 2006]. The standard data

[1]U.S. Geological Survey, Flagstaff, Arizona, USA.
[2]Department of Astronomy, Cornell University, Ithaca, New York, USA.
[3]Department of Geography, University of Winnipeg, Winnipeg, Manitoba, Canada.
[4]Planetary Science Institute, Tucson, Arizona, USA.
[5]Space Science Institute, Boulder, Colorado, USA.
[6]National Museum of Natural History, Smithsonian Institution, Washington, D. C., USA.
[7]Department of Earth and Planetary Sciences, Washington University, St. Louis, Missouri, USA.
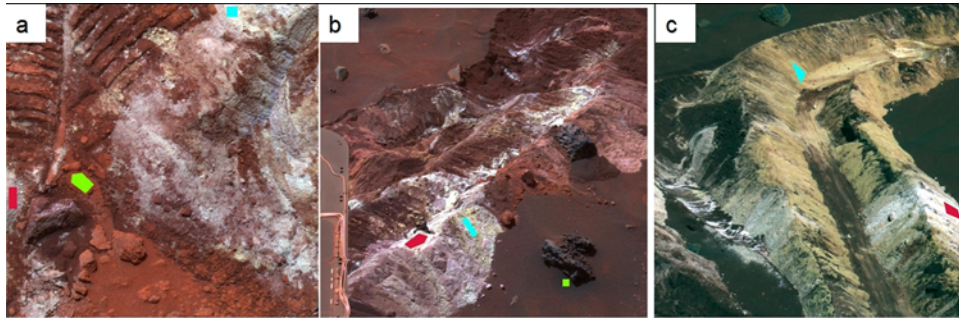[8]Jet Propulsion Laboratory, Pasadena, California, USA.

Figure 1. False-color (blue = 432 nm, green = 535 nm, red = 754 nm) images of (a) Paso Robles (Sol 400, P2551), field of view is ~25 cm; (b) Arad (Sol 721, P2538), field of view is ~60 cm; and (c) Tyrone (Sol 790, P2531), field of view is ~65 cm. Locations from which spectra were acquired are shown as follows: Paso Robles: red = "gray" soil, cyan = "white" soil, green = Paso Robles background soil. Arad: red = "white" soil, cyan = "yellow" soil, green = Arad basaltic soil. Tyrone: red = "white" soil, cyan = "yellow" soil.

reduction process removes a substantial portion of the diffuse illumination component of the Martian sky from Pancam spectra, particularly for surfaces inclined similarly to the calibration target. Although the spectra were not corrected further for diffuse illumination here, *Johnson et al.* [2006a] demonstrated that diffuse component corrections are relatively minor for the solar incidence angles of these data (14°−32°; Table 1).

2.2. Mixing Models

[6] We used a multiple end-member spectral mixture algorithm (MESMA) in combination with a spectral reference library composed of 84 laboratory spectra (Table 2): 63 sulfate and ferric oxide minerals [*Crowley et al.*, 2003;

Cloutis et al., 2006], three phosphate samples (ASTER JPL Spectral Library, 1998 http://speclib.jpl.nasa.gov/forms/asp/mineral.htm), 15 olivine, pyroxene, and plagioclase minerals [*Clark et al.*, 2003], and two Pancam spectra of typical background Gusev soil (Figure 1), plus the JSC-1 Mars analog soil [*Johnson and Grundy*, 2001]. MESMA-based algorithms have been used with visible/near-infrared data to map vegetation cover and soil types [*Sabol et al.*, 1992; *Roberts et al.*, 1998; *Okin et al.*, 2001; *Dennison et al.*, 2004], as well as the distribution and mixing between lunar mare and highland materials [*Li and Mustard*, 2003]. Our implementation of the MESMA algorithm builds on previous work using thermal infrared data [*Staid et al.*, 2004; *Johnson et al.*, 2006b]. The MESMA algorithm initially
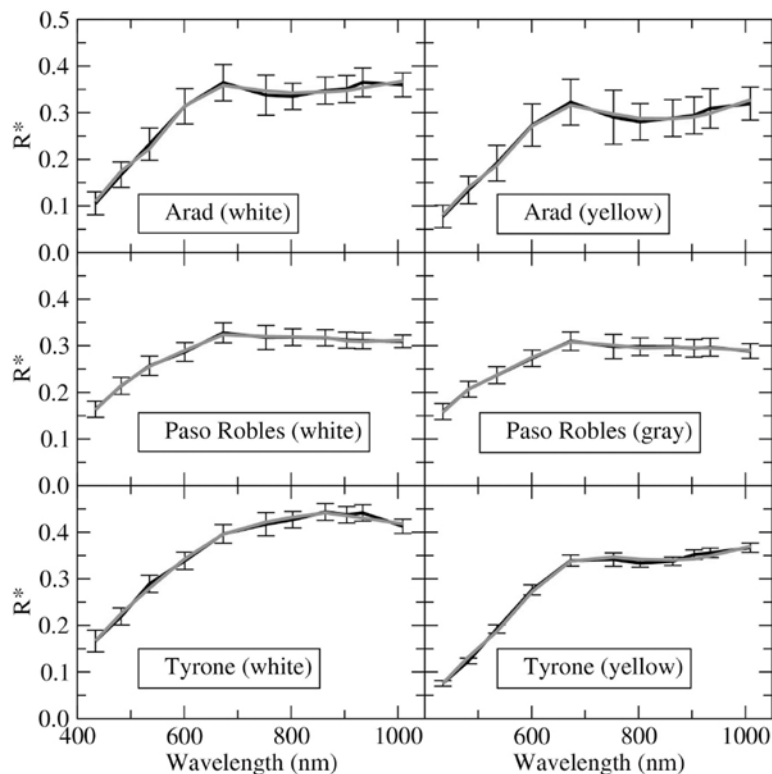

Figure 2. Pancam spectra (dark lines) extracted from regions of interest (ROI) shown in Figure 1; error bars are standard deviations of pixels in each ROI. MESMA modeled spectra (gray lines) overlain. See Table 3 for model results.

Table 1. Pancam Imaging Sequences Used in This Work

Area	Sol	Site	Position	Sequence ID	Local True Solar Time	First Exposure by Wheels, Sol	Incidence Angle, deg	Emission Angle,[a] deg	Phase Angle, deg
Paso Robles	400	106	0	P2551	13:31	398	32	85	34
Arad	721	122	267	P2538	11:40	719	14	45	67
Tyrone	790	126	142	P2531	11:58	782	27	28	42

[a]INSTRUMENT_ELEVATION.

compared all possible combinations of four mineral spectra from the reference library. The best model containing positive endmember abundances for each spectrum was identified via the RMS error computed for each combination: $RMS = sqrt[(\sum_{b=1}^{b} E^2)/b]$ where E is the difference between the Pancam and MESMA model spectrum at each band, and $b = 11$ Pancam bands. Then each unused reference library spectrum was alternately added to the existing endmember set and a new RMS error was computed for each combination. The spectrum that provided the best improvement (and was selected with a positive abundance for all endmember components) was then kept as an additional endmember. This procedure was then repeated until as many as eleven minerals were selected from the reference library, although the procedure was allowed to complete sooner if no additional positive-abundance endmember occurred that improved the RMS error. The algorithm produced fractions for each endmember along with RMS errors for each fit. We did not constrain the abundances to sum to 1.0, but we did normalize the modeled abundances to 100%, as has been typical in previous studies [e.g., *Li and Mustard*, 2003].

[7] We note that linear mixing models such as MESMA cannot be used directly to provide absolute abundances of mineral components owing to non-linear effects induced by intimate mixing (a particular problem with the disturbed soils analyzed here [e.g., *Clark*, 1983; *Clark and Roush*,

1984; *Mustard and Pieters*, 1987; *Poulet and Erard*, 2004]). Some workers have addressed this issue by converting reflectance measurements to single scattering albedo (where linear mixing is more applicable). However, such approximations assume that the materials scatter photons isotropically and exhibit no opposition effect [e.g., *Hapke*, 1993]. Although the observations used here were obtained far from zero phase angle (Table 1), nearly all soils at the Gusev site are backscattering [*Johnson et al.*, 2006a]. As such, we preferred to work with the R* values and assume that the models provide first-order constraints on mineral detections, if not absolute abundances. Given these constraints, we ran the MESMA algorithm for six Pancam spectra extracted from the regions in Figure 1. The modeled spectra are shown overlain on the Pancam spectra in Figure 2, and Table 3 lists the major minerals detected by the model, their fractional abundances, and the RMS errors of each model. Figure 3 shows the spectra (convolved to Pancam bandpasses) selected by the MESMA models.

3. Results

[8] The MESMA algorithm modeled the Pancam spectra relatively well using between 5 and 9 endmembers, with RMS errors <0.010 in all models (Figure 2 and Table 3). All Pancam spectra were modeled consistently with a large proportion of undisturbed soil and/or JSC-1 soil spectra (~40–60%). The Paso Robles soils were best modeled with small amounts (~10%) of paracoquimbite and fibroferrite,

Table 2. Reference Library Used in MESMA Models

Laboratory Spectra	Reference
Natrojarosite SPT107, Natroarosite SPT108, Ferricopiapite + Metavoltine SPT109, Rhomboclase SPT110, Voltaite + Romerite SPT111, Amarantite SPT112, Jarosite SPT113, Natrojarosite SPT114, Jarosite SPT115, Jarosite SPT116, Copiapite SPT117, Halotrichite SPT118, Coquimbite SPT119, Hydronium Jarosite SPT120, Fibroferrite SPT121, Romerite SPT122, Sideronatrite SPT123, Botryogen SPT124, Ferricopiapite SPT125, Coquimbite SPT126, Gypsum SPT127, Anhydrite + Gypsum SPT128, Alunite SPT129, Rozenite + Melanterite SPT130, Coquimbite SPT131, Anhydrite + Coquimbite SPT132, Ferricopiapite SPT133, Coquimbite + Romerite SPT134, Sideronatrite SPT136, Paracoquimbite SPT137, Copiapite SPT138, Rhomboclase SPT139, Pickeringite SPT140, Kieserite SPT141, Hexahydrite + Pickeringite SPT142, Hexahydrite SPT143, Szomolnokite + Rozenite SPT144, Anglesite SPT145, Barite SPT146, Anglesite SPT147, Anglesite SPT148, Lazurite SPT150, Lazurite SPT151, Lazurite SPT152, Lazurite SPT153, Synthetic Anhydrite PIG002, Synthetic Barite PIG003, Synthetic Gypsum PIG005, Synthetic Anglesite PIG021	*Cloutis et al.* [2006][a]
Copiapite, Ferricopiapite, Ferrihydrite, Goethite, Halotrichite, Hematite, Jarosite, Melanterite, Paracoquimbite, Pickeringite, Rhomboclase, Rozenite, Szmolnokite	*Crowley et al.* [2003][b]
Apatite (<45 μm), Apatite (45–125 μm), Apatite (125–500 μm)	ASTER JPL Spectral Library (1998)
Olivine GDS70 (Fo89; <60 μm), Olivine KI3005 (Fo11, <60 μm), Olivine KI3188 (Fo51; <60 μm), Hedenbergite NMNH1191197 (<200 μm), Diopside HS15 (295 μm), Augite WS592 (174 μm), Pigeonite HS199 (74–250 μm), Bronzite HS9 (260 μm), Hypersthene PYX02, (En86; >250 μm), Albite HS66 (74–250 μm), Anorthite GDS28 (74–250 μm), Bytownite HS106 (74–250 μm), Andesine HS142 (74–250 μm), Labradorite HS105 (74–250 μm), Oligoclase HS110 (74–250 μm)	*Clark et al.* [2003]
Paso Robles soil (Pancam), Arad basaltic soil (Pancam), JSC-1 analog soil [*Johnson and Grundy*, 2001]	*Soils*

[a]*Cloutis et al.* [2006] samples are <45 μm fractions.
[b]*Crowley et al.* [2003] sample fractions are 100–250 μm fractions.

Table 3. MESMA Model Results[a]

	Sample					
Endmember	Arad White	Arad Yellow	Paso Robles Gray	Paso Robles White	Tyrone White	Tyrone Yellow
Ferricopiapite $Fe_{2/3}^{3+}Fe_4^{3+}(SO_4)_6 (OH)_2 \cdot 20(H_2O)$	–	–	–	–	–	27
Paracoquimbite(SPT 137) $Fe_2^{3+}(SO_4)_3 \cdot 9(H_2O)$	–	–	7	6	7	–
Anhydrite + Coquimbite (SPT 132) $(CaSO_4) + Fe_2^{3+}(SO_4)_3 \cdot 9(H_2O)$	–	–	–	9	–	–
Fibroferrite $Fe^{3+}(SO_4) (OH) \cdot 5(H_2O)$	4	16	6	14	–	5
Hydronium jarosite(STP 120) $(H_3O)Fe_3^{3+}(SO_4)_2(OH)_6$	21	29	–	–	–	12
Rhomboclase $HFe^{3+}(SO_4)_2 \cdot 4(H_2O)$	9	–	–	–	–	3
Olivine$(Fe,Mg)_2 SiO_4$	–	–	11	–	–	–
Diopside $CaMg(Si_2O_6)$	–	5	–	–	17	–
Augite$(Ca,Na)(Mg,Fe,Al,Ti) (Si,Al)_2O_6$	–	–	12	31	20	–
Hedenbergite $CaFe(Si_2O_6)$	–	–	13	–	–	–
Oligoclase $(Na,Ca)(Si,Al)_4O_8$	–	–	4	–	–	–
Paso Robles soil	60	50	38	39	–	35
JSC-1 soil	–	–	11	–	55	18
RMS error	0.0071	0.0060	0.0013	0.0018	0.0056	0.0053

[a]Relative percent major minerals and soils.

along with larger amounts ($\sim$10–30%) of olivine and pyroxene. The white Paso Robles soil models also selected a small amount of an anhydrite + coquimbite mixture. The Tyrone white soil was modeled with mainly JSC-1 soil and pyroxenes and only a small amount (<10%) of paracoquimbite. However, the yellow Tyrone soil was modeled with no pyroxenes and a large amount ($\sim$50%) of hydrated sulfate minerals, including rhomboclase, fibroferrite, hydronium jarosite, and ferricopiapite [cf. *Friedlander et al.*, 2007], consistent with the 6 μm Mini-TES feature detected in Tyrone soils. The Arad soils were also modeled with moderate amounts of hydronium jarosite (>20%), in addition to smaller amounts of fibroferrite and rhomboclase. No phosphates were detected in any of the models, despite the $\sim$5% P_2O_5 abundances detected by the APXS instrument for the Paso Robles soil [e.g., *Yen et al.*, 2007] (also A. S. Yen et al., Aqueous Processes at Gusev Crater: An Evaluation of Paso Robles Class Soils, manuscript in preparation, 2007) (hereinafter referred to as Yen et al., manuscript in preparation, 2007). Ongoing work by Lane et al. also suggests that iron phosphates may be an important component of the Paso Robles soils (M. Lane and J. Bishop, personal communication, 2007).

4. Discussion

[9] The MESMA method can only detect the presence of mineral phases that are included in its reference library; thus, incomplete sampling of sulfate mineral phases (and grain size separates) is an important limitation on the interpretation of our results. Despite that limitation, however, we believe that the assembled sulfate mineral spectra represent a fairly comprehensive collection and that our results provide important insights regarding the identification and possible origin of the sulfates detected in Gusev crater. Specifically, our results suggest that although the disturbed light-toned soils are contaminated with "dusty" surface soils, their visible/near-infrared spectral features are consistent with variably hydrated ferric sulfates. Whereas the modeled abundances of background surface soils are larger than the amounts suggested by APXS and MB results [e.g., *Yen et al.*, 2007, manuscript in preparation, 2007], they are consistent with those modeled by *Lane et al.* [2006a, 2007] for the Paso Robles site using Mini-TES

data. However, the background soils may be favored by the models because they are relatively dark compared to the sulfate spectra, and darker materials tend to dominate spectral mixtures in these wavelengths [e.g., *Clark*, 1983].

[10] Three preliminary hypotheses may explain the origin of the bright Gusev subsurface soils: 1) Evaporation of salty ground and/or surface water with subsequent precipitation of sulfate minerals [e.g., *Wang et al.*, 2006]; 2) Subaerial reaction of widespread SO_2-rich volcanic aerosols with the surfaces of basaltic rocks and soils [e.g., *Settle*, 1979]; or 3) Condensation/precipitation of sulfur-bearing minerals from the percolation of subsurface fumarole/sulfatara gases [e.g., *Goff and Janik*, 2000; Yen et al., manuscript in preparation, 2007].
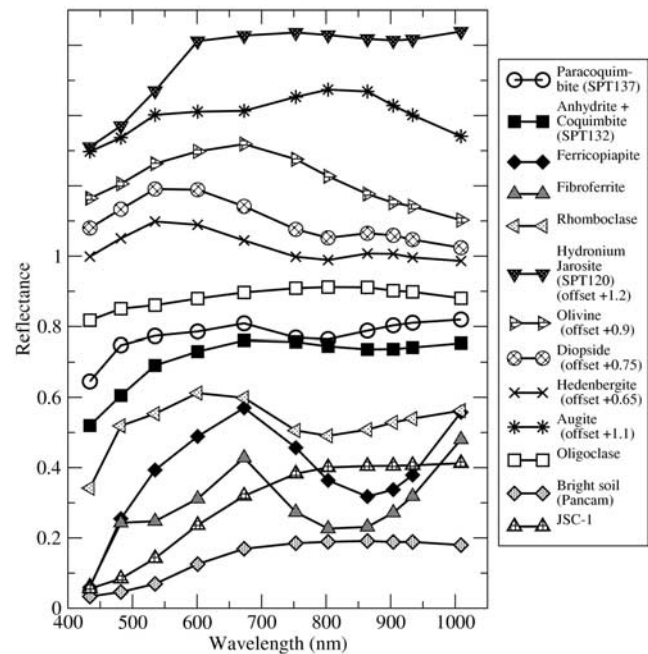

Figure 3. Laboratory spectra (convolved to Pancam bandpasses) of minerals selected by MESMA models of sulfur-rich soil spectra shown in Figure 2 (cf. Table 3), along with "Bright soil" (green ROI in Paso Robles area in Figure 1) and JSC-1 analog soil also selected by MESMA. Note offsets applied to selected spectra (see legend).

Evaporite deposits could be expected to show a compositional gradient with depth that would support a model of sulfate precipitation from fluids [*Wang et al.*, 2007]. The geomorphic setting of the Arad and Tyrone sites in topographic depressions is consistent with the materials forming elsewhere and accumulating at these sites by aeolian transport. In contrast, deposits created by regionally-distributed surface-volcanic aerosol reactions might have a broader distribution. Deposition by fumaroles could imply a local volcanic origin and the reaction of SO_2, water vapor, and other volatile gases with basaltic rock material and/or tephra deposits (e.g., those associated with the Home Plate structure). More thorough analyses using Spirit's entire suite of instruments in conjunction with orbital data are needed to understand the more detailed context and geologic history of these deposits. For example, determining their composition and mineralogy could provide strong constraints (e.g., pH, Eh, temperature) on the fluids or gases from which these deposits formed, and the degree to which impact mixing may have played a role in the evolution of these materials.

5. Conclusions

[11] We used a multiple endmember spectral mixture model to analyze Pancam spectra acquired from representative locations on light-toned disturbed soils at three locations along the MER Spirit rover traverse. The combined presence of relatively uncommon Pancam spectral features (670 nm reflectance maximum, 800–860 nm absorptions) suggest that hydrated ferric sulfates are a significant component in these soils. *Wang et al.* [2007] are investigating an apparent temporal change in Pancam spectra of the yellow Tyrone soils, perhaps indicative of dehydration of exposed ferric sulfate minerals. More detailed analyses using the entire suite of instruments aboard Spirit are underway to further constrain the variable mineralogy of these soils [e.g., *Lane et al.*, 2006b, 2007]. Preliminary results suggest a wide variety of candidate hydrated ferric sulfate minerals detected by the different instruments. However, such variability may be consistent with the extreme spatial heterogeneity over short length and depth scales [e.g., *Yen et al.*, 2007, manuscript in preparation, 2007] observed thus far in these deposits.

References

Bell, J. F., III, et al. (2003), The Mars Exploration Rover Athena panoramic camera (Pancam) investigation, *J. Geophys. Res.*, *108*(E12), 8063, doi:10.1029/2003JE002070.

Bell, J. F., III, J. Joseph, J. N. Sohl-Dickstein, H. M. Arneson, M. J. Johnson, M. T. Lemmon, and D. Savransky (2006), In-flight calibration and performance of the Mars Exploration Rover panoramic camera (Pancam) instruments, *J. Geophys. Res.*, *111*, E02S03, doi:10.1029/2005JE002444.

Bishop, J. L., et al. (2006), VNIR spectra of sulfates formed in solfataric and aqueous acid sulfate environments and applications to Mars, paper presented at Workshop on Martian Sulfates as Recorders of Atmospheric-Fluid-Rock Interactions, Lunar and Planet. Inst., Houston, Tex.

Clark, R. N. (1983), Spectral properties of mixtures of montmorillonite and dark carbon grains: Implications for remote sensing minerals containing chemically and physically adsorbed water, *J. Geophys. Res.*, *88*, 10,635–10,644.

Clark, R. N., and T. L. Roush (1984), Reflectance spectroscopy: Quantitative analysis techniques for remote sensing applications, *J. Geophys. Res.*, *89*, 6329–6340.

Clark, R. N., et al. (2003), USGS Digital Spectral Library splib05a [online], *U.S. Geol. Surv. Open File Rep., 03-395*. (Available at http://purl. access.gpo.gov/GPO/LPS43304)

Cloutis, E. A., et al. (2006), Detection and discrimination of sulfate minerals using reflectance spectroscopy, *Icarus*, *184*, 121–157.

Crowley, J. K. (2003), Spectral reflectance properties (0.4–2.5 μm) of secondary Fe-oxide, Fe-hydroxide, and Fe-sulphate-hydrate minerals associated with sulphide-bearing mine wastes, *Geochem. Explor. Environ. Anal.*, *3*, 219–228.

Dennison, P. E., K. Q. Halligan, and D. A. Roberts (2004), A comparison of error metrics and constraints for multiple endmember spectral mixture analysis and spectral angle mapper, *Remote Sens. Environ.*, *93*, 359–367.

Friedlander, L. R., N. J. Tosca, and R. E. Arvidson (2007), Preliminary experiments in the systematic investigation of the spectroscopic properties of synthetic copiapite group minerals, *Lunar Plan. Sci.*, *XXXVIII*, abstract 2049.

Gellert, R., et al. (2006), Alpha particle X-ray spectrometer (APXS): Results from Gusev crater and calibration report, *J. Geophys. Res.*, *111*, E02S05, doi:10.1029/2005JE002555.

Goff, F., and C. J. Janik (2000), *Geothermal Systems*, pp. 817–834, Academic Press, San Diego, Calif.

Hapke, B. (1993), *Theory of Reflectance and Emittance Spectroscopy*, 455 pp., Cambridge Univ. Press, New York.

Johnson, J. R., and W. M. Grundy (2001), Visible/near-infrared spectra and two-layer modeling of palagonite-coated basalts, *Geophys. Res. Lett.*, *28*, 2101–2104.

Johnson, J. R., et al. (2006a), Spectrophotometric properties of materials observed by Pancam on the Mars Exploration Rovers: 1. Spirit, *J. Geophys. Res.*, *111*, E02S14, doi:10.1029/2005JE002494.

Johnson, J. R., M. I. Staid, T. N. Titus, and K. Becker (2006b), Shocked plagioclase signatures in Thermal Emission Spectrometer data of Mars, *Icarus*, *180*, 60–74.

Lane, M. D., et al. (2006a), Determining the chemistry of the bright Paso Robles soils on Mars using multispectral data sets, paper presented at Martian Sulfates as Recorders of Atmospheric-Fluid-Rock Interactions, Lunar and Planet. Inst., Houston, Tex.

Lane, M. D., et al. (2006b), Laboratory emission, visible-near infrared, and Mössbauer spectroscopy of iron sulfates: Application to the bright Paso Robles soils in Gusev crater, Mars, *Lunar Planet. Sci.*, *XXXVII*, abstract 1799.

Lane, M. D., et al. (2007), Identifying the phosphate and ferric sulfate minerals in the Paso Robles soils (Gusev crater, Mars) using an integrated spectral approach, *Lunar Planet. Sci.*, *XXXVIII*, abstract 2176.

Li, L., and J. F. Mustard (2003), Highland contamination in lunar mare soils: Improved mapping with multiple end-member spectral mixture analysis (MESMA), *J. Geophys. Res.*, *108*(E6), 5053, doi:10.1029/2002JE001917.

Maki, J. N., et al. (2003), The Mars Exploration Rover engineering cameras, *J. Geophys. Res.*, *108*(E12), 8071, doi:10.1029/2003JE002077.

Ming, D. W., et al. (2006), Geochemical and mineralogical indicators for aqueous process in the Columbia Hills of Gusev crater, Mars, *J. Geophys. Res.*, *111*, E02S12, doi:10.1029/2005JE002560.

Morris, R. V., et al. (2006), Mössbauer mineralogy of rock, soil, and dust at Gusev crater, Mars: Spirit's journey through weakly altered olivine basalt on the plains and pervasively altered basalt in the Columbia Hills, *J. Geophys. Res.*, *111*, E02S13, doi:10.1029/2005JE002584.

Mustard, J. F., and C. M. Pieters (1987), Quantitative abundance estimates from bidirectional reflectance measurements, *J. Geophys. Res.*, *92*, 617–626.

Okin, G., D. Roberts, B. Murray, and W. Okin (2001), Practical limits on hyperspectral vegetation discrimination in arid and semiarid environments, *Remote Sens. Environ.*, *77*, 212–225.

Parente, M., J. L. Bishop, and J. F. Bell III (2007), Spectral unmixing for sulfate identification in Pancam images, *Lunar Planet. Sci.*, *XXXVIII*, abstract 1934.

Poulet, F., and S. Erard (2004), Nonlinear spectral mixing: Quantitative analysis of laboratory mineral mixtures, *J. Geophys. Res.*, *109*, E02009, doi:10.1029/2003JE002179.

Reid, R. J., et al. (1999), Imager for Mars Pathfinder (IMP) image calibration, *J. Geophys. Res.*, *104*, 8907–8926.

Roberts, D. A., et al. (1998), Mapping Chaparral in the Santa Monica mountains using multiple endmember spectral mixture models, *Remote Sens. Environ.*, *65*, 267–269.

Sabol, D. E., et al. (1992), Quantitative subpixel spectral detection of targets in multispectral images, *J. Geophys. Res.*, *97*, 2659–2672.

Settle, M. (1979), Formation and deposition of volcanic sulfate aerosols on Mars, *J. Geophys. Res.*, *84*, 8343–8354.

Sohl-Dickstein, J., et al. (2005), Modeling visible/near-infrared photometric properties of dustfall on a known substrate, *Lunar Planet Sci.*, *XXXVI*, abstract 2235.

Staid, M. I., J. R. Johnson, and L. R. Gaddis (2004), Analysis of Mars Thermal Emission Spectrometer data using large mineral reference libraries, *Lunar Plan. Sci.*, *XXXV*, abstract 1778.

Wang, A., et al. (2006), Sulfate deposition in subsurface regolith in Gusev crater, Mars, *J. Geophys. Res.*, *111*, E02S17, doi:10.1029/2005JE002513.

Wang, A., J. F. Bell III, and R. Li (2007), Salty soils at Gusev Crater as revealed by Mars Exploration Rover Spirit, *Lunar Plan. Sci.*, *XXXVIII*, abstract 1196.

Yen, A. S., et al. (2007), Composition and formation of the "Paso Robles" class soils at Gusev Crater, *Lunar Plan. Sci.*, *XXXVIII*, abstract 2030.

————————————

J. F. Bell III and M. Rice, Cornell University, 402 Space Sciences Building, Ithaca, NY 14853, USA. (jfb8@cornell.edu; mrice@astro.cornell.edu)

E. Cloutis, Department of Geography, University of Winnipeg, 515 Portage Avenue, Winnipeg, Manitoba, Canada R3B 2E9. (e.cloutis@uwinnipeg.ca)

W. H. Farrand, Space Science Institute, 4750 Walnut Street, Suite 205, Boulder, CO 80301, USA. (farrand@colorado.edu)

J. R. Johnson, U.S. Geological Survey, 2255 North Gemini Drive, Flagstaff, AZ 86001, USA. (jrjohnson@usgs.gov)

T. McCoy, National Museum of Natural History, Smithsonian Institution, 10th and Constitution Avenues, NW, Washington, DC 20560, USA. (mccoyt@si.edu)

M. Staid, Planetary Science Institute, 1700 E. Ft. Lowell Rd., Suite 106, Tucson, AZ 85719, USA. (staid@psi.edu)

A. Wang, Department of Earth and Planetary Sciences, Campus Box 1169, One Brookings Drive, Washington University, St. Louis, MO 63130, USA. (alianw@levee.wustl.edu)

A. Yen, Jet Propulsion Laboratory, Mail Code 183-501, 4800 Oak Grove Drive, Pasadena, CA 91109, USA. (albert.yen@jpl.nasa.gov)